Chapter 8

Infrared Solar Thermal-Shielding Applications Based on Oxide Semiconductor Plasmonics

Hiroaki Matsui and Hitoshi Tabata

Additional information is available at the end of the chapter

http://dx.doi.org/10.5772/67588

Abstract

This chapter describes plasmonic responses in In_2O_3:Sn nanoparticles (ITO NPs) and their assembled ITO NP sheets in the infrared (IR) range. ITO NPs clearly provide resonance peaks related to local surface plasmon resonances (LSPRs) in the near-IR range, which are dependent on electron density in the NPs. In particular, electron-impurity scattering plays an important role in determining carrier-dependent plasmon damping, which is needed for the design of plasmonic materials based on ITO. ITO NPs are mainly dominated by light absorption. However, a high light reflection is observed in the near- and mid-IR range when using assembled NP sheets. This phenomenon is due to the fact that the introduction of surface modifications to the NPs can facilitate the production of electric-field (*E*-field) coupling between the NPs. The three-dimensional (3*D*) *E*-field coupling allows for resonant splitting of plasmon excitations to the quadrupole and dipole modes, thereby obtaining selective high reflections in the IR range. The high reflective performances from the assembled NP sheets were attributed to the plasmon interactions at the internanoparticle gaps. This work provides important insights for harnessing IR optical responses based on plasmonic technology toward the fabrications of IR solar thermal-shielding applications.

Keywords: oxide semiconductor, surface plasmon, infrared and energy-saving

1. Introduction

Plasmonic nanomaterials based on transparent oxide semiconductors (TOSs, such as In_2O_3, ZnO and SnO_2) have received much attention as new optical phenomena with potential applications. In particular, oxide semiconductors with metallic conductivity by doping with

intrinsic and/or extrinsic impurities show surface plasmon resonances (SPRs) in the infrared (IR) range [1–5]. Unlike noble metals (silver and gold), SPRs can be controlled by tuning the physical characters of a material [6–8], which provides new possibilities for optical manipulation of light. Studies of nanoplasmonics based on TOSs can break new ground in the areas of oxide semiconductors. A characteristic property cleared by these studies is that the optical nature of TOSs shows a low-loss plasmonic material even up to near-IR wavelengths because of IR transparency outside the reststrahlen band. The band structures on TOSs are simply composed of *s*- and *p*-orbitals [9], indicating no inter band transition-related *d*-orbitals such as those exhibited by the noble metals [10]. TOS materials with metallic conductivity have mainly applied to transparent electrodes [11, 12]. Therefore, SPRs on TOSs provide new insight for alternative plasmonic applications in the IR range.

SPR excitations on TOSs have been reported on different structures such as nanorods and nanowires [13–15]. In particular, nanoparticles (NPs) of In_2O_3:Sn and ZnO:Al produce localized surface plasmon resonances (LSPRs), which are strongly generated when confining the collective excitations of carriers into NPs [16, 17]. This makes use of localization of large electric fields in the vicinity of NP surfaces. Thus far, the majority of investigations concerning LSPRs have demonstrated on the noble metal NPs, which have been tailored for use in optical areas as diverse as waveguides and biochemical sensing [18–20]. Recently, In_2O_3:Sn NPs have launched as nanoplamonic materials. The careful choice of impurity dopants can show clear LSPR peaks in the near-IR range. The assembled films of In_2O_3:Sn NPs have shown optical enhancements of near-IR luminescence and absorption [21, 22]. These behaviours make use of the electric-fields (*E*-fields) excited on the NP film surfaces [23].

Assembled films of the noble metals have been utilized in surface-enhanced Raman and fluorescence spectroscopies, which are based on high *E*-fields derived from plasmon coupling between the NPs. When metal NPs are located near one another, coupling LSPR induces in a gap between NPs [24]. The strength of LSPR enhances with the magnitude due to interparticle coupling. This optical phenomenon has been utilized in enhanced light emissions, for example, hybrid layers of silver NPs and InGaN/GaN quantum wells [25]. However, assembled films of metal NPs have been limited in the visible range. The use of TOSs extends to longer wavelengths in the IR range.

Plasmonic properties of TOS materials have attracted attention for thermal-shielding applications in order to solar and radiant heat in the near- and mid-IR range, respectively [26]. To date, the composites and films of oxide semiconductor NPs have been studied regard to transmission and extinction spectra in the IR range because optical properties are dominated by absorbance [27–30]. The present thermal-shielding applications have strongly been desired to cut IR radiation not by absorption but through reflection. However, no previous paper has reported reflective performance on doped oxide semiconductor NPs. In addition, plasmonic applications exhibiting a thermal-shielding ability have not been previously studied in detail. The purpose of this chapter is to apply the plasmonic properties for satisfying recent industry demands for a material with thermal-shielding ability. These social requirements include the fabrication of flexible sheets with high heat-ray reflections, as well as visible and microwave transmissions. We use assembled NPs of In_2O_3:Sn as a concrete example. Plasmonic responses are dependent on electronic structure. For example, In_2O_3, ZnO and WO_3 have similar band structures with

http://dx.doi.org/10.5772/67588

conduction and valence levels consisting of *s*- and *p*-orbitals. This indicates that the plasmonic properties of these materials can be well manipulated through same optical mechanism.

This chapter is organized as follows. In Section 2, we give a description of structural and optical properties of In_2O_3:Sn (ITO) NPs in the IR range from the viewpoint of local structural analyses. In Section 3, we focus plasmonic responses of ITO NPs from theoretical and experimental approaches, which is not as readily available in the noble metal NPs. To investigate mechanism of plasmonic excitations in ITO, NPs is valuable information for oxide-based plasmonics. Section 4 is devoted to discussion of thermal-shielding based on assembled films of ITO NPs for industrial applications. Above all, we describe plasmonic responses related to the 3*D* E-field coupling along the out-of-plane and in-plane directions. This has a key factor in producing selective high reflections in the IR Range, which provides important insights for harnessing IR optical properties towards the fabrications of solar-thermal shielding. In Section 5, we shortly provide electromagnetic (EM) responses of assembled ITO NP films in the microwave region. Finally, some concluding remakes are given in Section 6.

2. Fabrications and structures of ITO NPs

2.1. Fabrications of ITO NPs

In_2O_3:Sn nanoparticles (ITO NPs) were fabricated using a metal organic decomposition method. Various initial ratios of the metal precursor complexes of $(C_9H_{22}CO_2)_3In$ and $(C_9H_{22}CO_2)_4Sn$ were prepared as starting materials. Indium and tin carboxylates were heated with a chemical ratio of 95:5 in a flask supported by a mantle heater to 350°C. The temperature was maintained for 4 hours, and then the mixture was cooled to room temperature around 30°C. The obtain solutions produced a pale blue suspension, to which excess ethanol was introduced to cause precipitation. Centrifugation and repeated washing processes were carried out several times using ethanol, producing dried powders of ITO NPs with a pale blue colour. As a final step, the NP samples were dispersed in a nonpolar solvent of toluene. A zeta-potential measurement revealed that the NPs showed non-aggregated states in the solvent due to an electrostatic repulsion. The Sn concentration in the NPs in this chapter was measured by X-ray florescence spectroscopy.

2.2. Structural properties of ITO NPs

X-ray diffraction (XRD) measurements clarified that the NPs showed broad peaks characteristic of a colloidal sample with a crystal structure [**Figure 1(a)**] [31]. The *a*-axis length increased from 10.087 to 10.152 Å as a consequence of incorporations of Sn atoms in the host. Furthermore, local structures of the NPs were evaluated by transmission electron microscopy (TEM) [inset of **Figure 1(a)**]. The electron diffraction (ED) analyses revealed that the lattice interval (d_{222}) along the [222] direction at the centre region (d_{222} = 0.301 nm) was close to that at the edge region in the NP (d_{222} = 0.302 nm) [inset of **Figure 1(b)**]. In addition, the experimental results of energy-disperse X-ray microscopy showed that the Sn concentration [Sn] at the centre region,

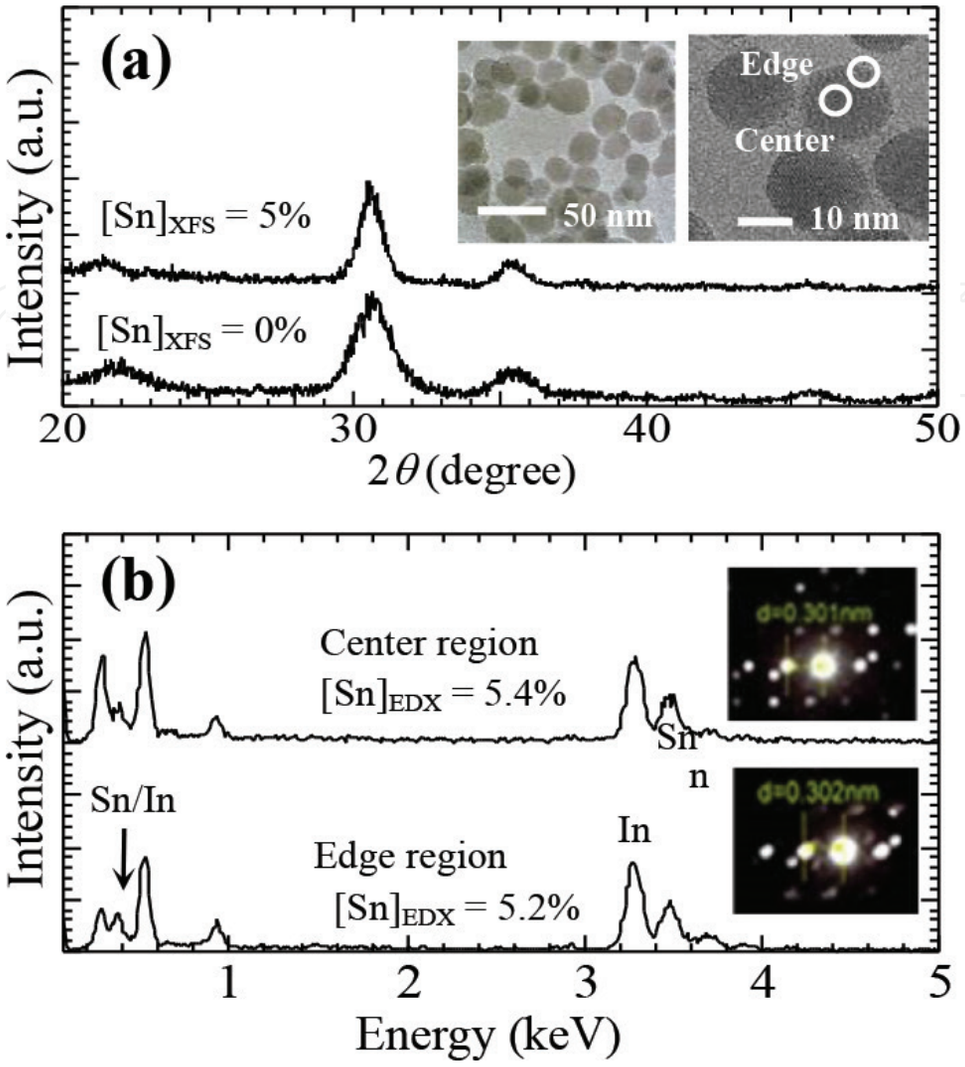

Figure 1. (a) XRD patterns of ITO NPs with Sn contents of 0 and 5%. Inset shows low-resolution (left) and high-resolution (right) TEM images of an ITO NP with a Sn content of 5%. (b) EDX spectra at the centre and edge regions in the NP. Inset represents ED patterns of the (222) plane at the centre and edge (Figure 1 of Ref. [22]). Copyright 2014 by the American Institute of Physics.

[Sn] = 5.4%, was similar to that at the edge region, [Sn] = 5.2%, which indicated that Sn atoms in the NP were spatially homogeneous [**Figure 1(b)**]. The NP diameter was around 20 nm, as confirmed using TEM and dynamic light-scattering methods. However, crystalline sizes derived from Scherer's equation from the (222) diffraction peak of XRD patterns were calculated as 1.58 and 2.20 nm for un-doped and doped NPs, respectively. Broadenings of the line-widths of the XRD patterns are attributed to structural imperfections such as defects and strains [22].

We further investigated structural properties by scanning-TEM (STEM) combined with electron-energy loss spectroscopy (EELS) [32]. A STEM-EELS technique can easily detect plasmonic response in a single NP. High-angle annular dark field (HAADF) images in **Figure 2(a)–(c)** cleared that Indium and Sn atoms in the NP were distributed homogeneously, which were consisted with the results of XRD. The EELS spectra at an edge and vacuum

http://dx.doi.org/10.5772/67588

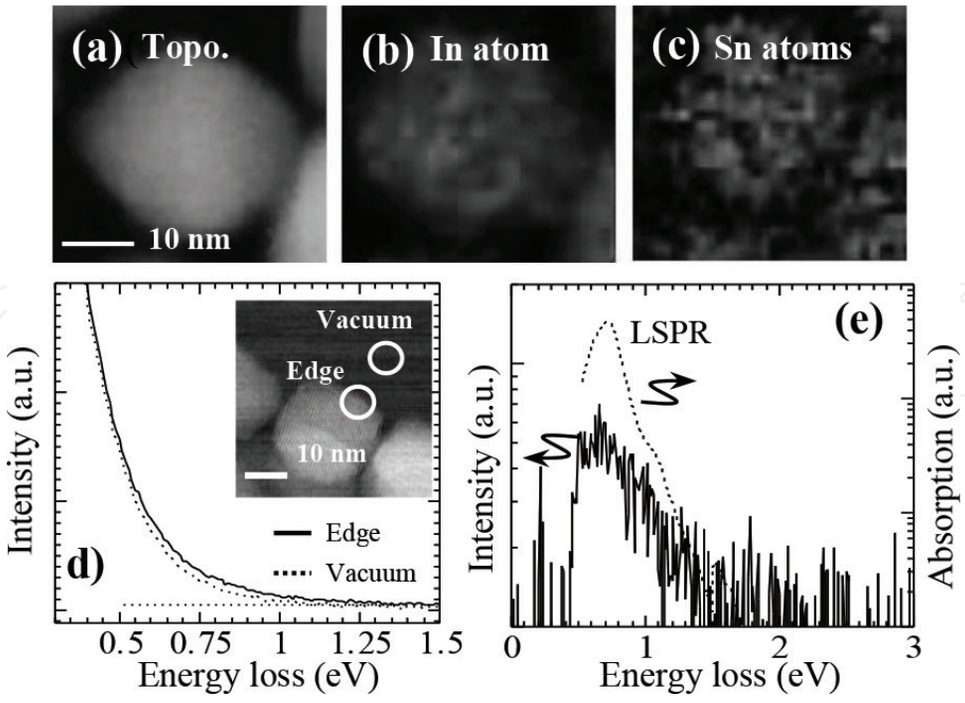

Figure 2. (a) Aberration-corrected STEM image, and HAADF images of In (b) and Sn atoms (c) in the ITO NP with a Sn concentration of 5%. (d) EELS spectra taken in the electron Probe position at vacuum (dotted line) and edge (solid line) regions, and a STEM-acquired particle image (inset). (e) Differential EELS spectrum (dotted line) and optical spectrum of ITO NP taken in the near-IR (solid line) (Figure 3 of Ref. [33]). Copyright 2014 by the American Institute of Physics.

region on the STEM-acquired particle image showed a slight spectral difference in energy-loss regions from 1.0 to 0.5 eV [**Figure 2(d)**]. In **Figure 2(e)**, a differential EELS spectrum had a maximum peak at 0.7 eV that was similar to the optical absorption in the near-IR, which was direct evidence of a LSP excitation on the NP surface as consequence of spatially homogeneous doping of Sn atoms in the NP.

3. Localized surface plasmons in ITO NPs

3.1. Theoretical calculations of optical properties

The absorption and scattering cross sections of a single ITO NP with a diameter (R) of 20 nm were theoretically estimated according to Mie theory on the basis of dielectric constants of a NP and a surrounding medium. A numerically analytical solution to Maxwell's equations describes the extinction (σ_{sca}) and scattering (σ_{scat}) of light by a perfect spherical particle structure as follows [34].

$$\sigma_{sca} = \frac{2\rho}{|k|^2} \sum_{L=1}^{\infty} (2L+1)\,(|a_L|^2 + |b_L|^2) \tag{1}$$

$$\sigma_{ext} = \frac{2\rho}{|k|^2} \sum_{L=1}^{\infty} (2L+1)\,[\,Re(a_L + b_L)\,] \tag{2}$$

where k is the incoming wave vector and L comprises integers representing the dipole, quadrupole, and high multipoles. a_L and b_L are represented by the following parameters, composed of the Riccati-Bessel equations of φ_L and δ_L:

$$a_L = \frac{m\,\varphi_L(mx)\,\varphi'_L(x) - \varphi'_L(mx)\,\varphi_L(x)}{m\,\varphi_L(mx)\,\delta'_L(x) - \varphi'_L(mx)\,\delta_L(x)} \tag{3}$$

$$b_L = \frac{\varphi_L(mx)\,\varphi'_L(x) - m\,\varphi'_L(mx)\,\varphi_L(x)}{\varphi_L(mx)\,\delta'_L(x) - m\,\varphi'_L(mx)\,\delta_L(x)} \tag{4}$$

where, $m = (n_R + in_I)/n_m$ is the complex refractive index of the metal, and n_m is the refractive index of the surrounding medium. In addition, $x = k_m r$ (r: is the radius of the particle). $k_m = 2\pi/\lambda_m$ is defined as the wavenumber in the medium. λ_m is the wavelength in the medium. **Figure 3(a)** shows absorption and scattering cross sections of an ITO NP with an R value of 20 nm. A peak position of LSP was located at around 1.8 μm. A spectral line-shape was a symmetric feature. A value of σ_{abs} was remarkably larger by three orders of magnitudes compared to σ_{scat}. The ratio of $\sigma_{abs}/\sigma_{scat}$ was not less than one for the particle diameter range above 200 nm [**Figure 3(b)**]. Therefore, it is considered that an ITO NP is dominated by light absorption in the near-IR region, indicating that it is not capable of light scattering an incident light in the near-IR range. Herein, we note that Full Mie theory in Eqs. (1)–(4) only has two functions of a dielectric constant and a particle diameter. The optical factors such as surface and radiation damping are excluded on the calculated spectra.

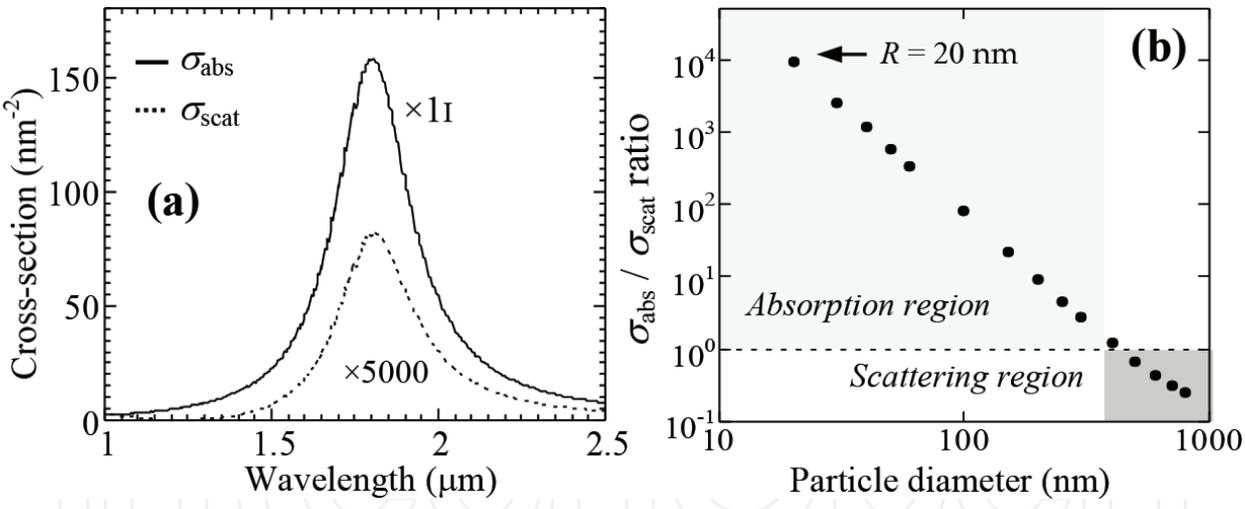

Figure 3. (a) Light absorption (σ_{abs}) and scattering (σ_{scat}) cross-sections of an ITO NP with an R value of 20 nm. (b) A value of $\sigma_{abs}/\sigma_{scat}$ ratio as a function of particle diameter.

3.2. Experimental optical properties

An optical absorption of an ITO NP solution (Sn concentration of 5%) was typically examined [**Figure 4(a)**]. Optical measurements in the IR-range were made at room temperature using a FT-IR spectrometer equipped with a liquid cooled HgCdTe (MCT) detector. An ITO NP solution was confined in an IR-transparent CaF_2 holder with an optical thickness of 25 μm, showing that a single absorption peak was located at 1.86 μm because of LSP excitations of

http://dx.doi.org/10.5772/67588

ITO NPs. This result was close to the theoretical data. We studied optical quality in plasmon resonances of ITO NPs using Mie theory as follows.

The absorption spectrum was fitted using the classical Mie theory with plasmon damping γ because of ionized impurity scattering derived from Sn impurities in the NPs. The theoretical fitting of an optical absorption (σ) to the experimental data in the quasi-static limit was employed [34]:

$$\sigma = 4\pi k R^3 \, Im\left\{\frac{\varepsilon_p(\omega)-\varepsilon_H}{\varepsilon_p(\omega)+2\varepsilon_H}\right\} \tag{5}$$

where, $k = 2\pi(\varepsilon H)^{1/2}\,\omega/c$ with c representing the speed of light, $\varepsilon_p(\omega)$ is the particle dielectric function, R is the particle radius, and ε_H indicates the host dielectric constants of toluene. The effective dielectric function (ε_{eff}) was used to obtain real nanoparticle dispersion by the Maxwell-Garnett effective medium approximation [35]:

$$\frac{\varepsilon_{eff}(\omega)-\varepsilon_H}{\varepsilon_{eff}(\omega)+2\varepsilon_H} = f_v \frac{\varepsilon_p(\omega)-\varepsilon_H}{\varepsilon_p(\omega)+2\varepsilon_H} \tag{6}$$

where, f_v is the particle volume fraction in the order of 10^{-5}. $\varepsilon_p(\omega)$ used the free-electron Drude term with a damping constant (γ) because ITO consists of free electrons due to the absence of interband transitions:

$$\varepsilon_p(\omega) = 1 - \frac{\omega_p^2}{\omega(\omega + i\gamma)} \tag{7}$$

The plasma frequency (ω_p) is defined to $\omega_p = n_e/\varepsilon_\infty\varepsilon_0 m^*$, where ε_∞ is the high-energy dielectric constant, and m^* is the effective electron mass. The fitted absorption was used with parameter values of $\varepsilon_H = 2.23$, $m^* = 0.3m_0$ and $\varepsilon_\infty = 3.8$ to determine $\varepsilon_p(\omega)$. In **Figure 4(a)**, the experimental absorption spectrum of the ITO NP solution could not be fitted to Mie theory based on Eqs. (1)–(3).

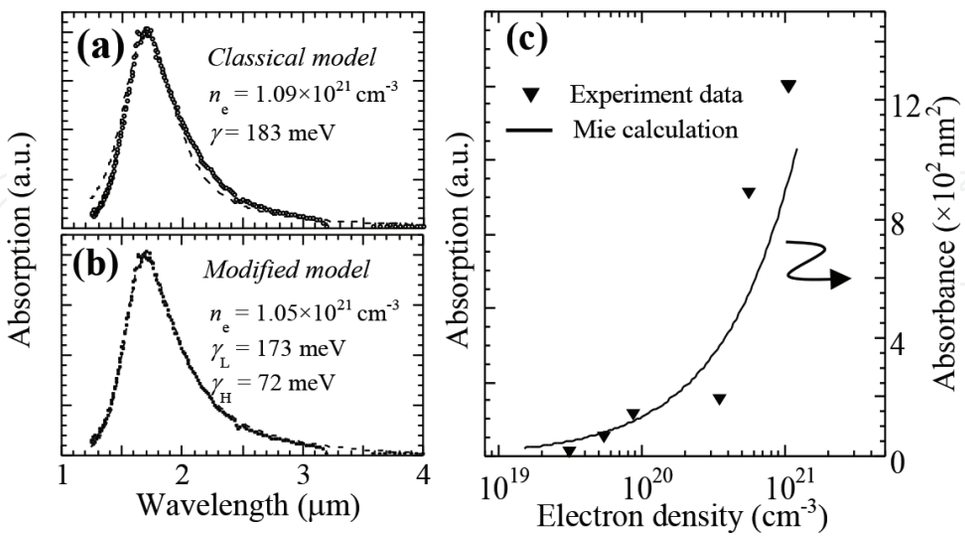

Figure 4. Experimental absorption spectrum of an ITO NP solution (Sn concentration of 5%) fitted to the classical (a) and modified Mie theory (b). Experimental and calculated spectra were indicated by open circles and dotted lines. (c) Absorption intensity of solution with ITO NPs with different electron density (black dots). Comparative data (black line) was extracted from the calculated absorption.

In general, plasmon damping γ of metallic NPs has been defined as a constant value. That is, γ is independent on frequency. However, plasmon damping of oxide semiconductors have been strongly dependent on frequency due to presence of electron-impurity scattering in a host. This is an interesting feature of the plasmonic response in doped oxide semiconductor NPs. Elucidation of the carrier-dependent damping mechanism is required for the design of plasmonic materials on TOSs. Therefore, frequency-dependent $\gamma(\omega)$ is introduced into the Drude term [36]. This is treated as the modified Mie theory for applying to doped oxide semiconductors.

$$\gamma(\omega) = f(\omega)\,\gamma_L + [\,1 - f(\omega)\,]\gamma_H\left(\frac{\omega}{\gamma_H}\right) \tag{8}$$

$$f(\omega) = \frac{1}{1 + exp\left(\frac{\omega - \gamma_X}{\sigma}\right)} \tag{9}$$

Above all, γ_L has information concerning electron-impurity scattering, resulting in an asymmetric spectral feature followed by spectral broadening in the long wavelength region [**Figure 4(b)**]. That is, it is considered that ionized impurity scattering attributed to Sn impurities in the NPs provided the asymmetric LSP response. In addition, strength in plasmon absorption remarkably increased with Sn concentration, as supported from experimental and theoretical aspects [**Figure 4(c)**]. LSPRs of ITO NPs were observed in electron density region above 3×10^{19} cm^{-3}, which was close to Mott critical density ($N_c = 9 \times 10^{18}$ cm^{-3}) of ITO. Above the N_c of ITO, the Fermi energy is determined by the highest occupied states in the conduction band. That is, LSP excitations are required to realize metallic states in the NPs, and became very strong at high electron densities above 10^{21} cm^{-3}.

4. Fabrications and structures of ITO NP sheets

4.1. Fabrications

Assembled NP sheets were deposited on IR transparent CaF_2 substrates by a spin-coating technique. Thick NP sheets were fabricated by way of multiple overglaze of a thin NP film obtained by a NP concentration of 0.2% in toluene. The spin-coating conditions were carried out using the following processes: 800 rpm (5 seconds) → 1200 rpm (10 seconds) → 2400 rpm (30 seconds) → 800 rpm (10 seconds). Fabricated sheet samples were heat-treated at above 150°C in air in order to evaporate the solvent. NP sheets with various thicknesses were obtained by repetition of the above coating sequences.

4.2. Structural evaluations

The assembled sheets of the NPs were evaluated by small-angle X-ray scattering (SAXS), providing an interesting insight into the scattering vector (q) of the SAXS intensity. A maximum SAXS peak (q_{max}) includes structural information about spatial ordering of nanoparticles estimated using $l = 2\,\pi/q_{max}$ with a spatial period (l). The SAXS pattern showed a maximum peak at $q = 0.33$ nm^{-1} followed with weak interferences [**Figure 5(a)**]. This resulted in an l value of 20 nm being close to the edge-to-edge between NPs, which was confirmed from in-plane surface scanning microscopy (SEM). A SEM image showed a close-packed structure because spin-coating produces

http://dx.doi.org/10.5772/67588

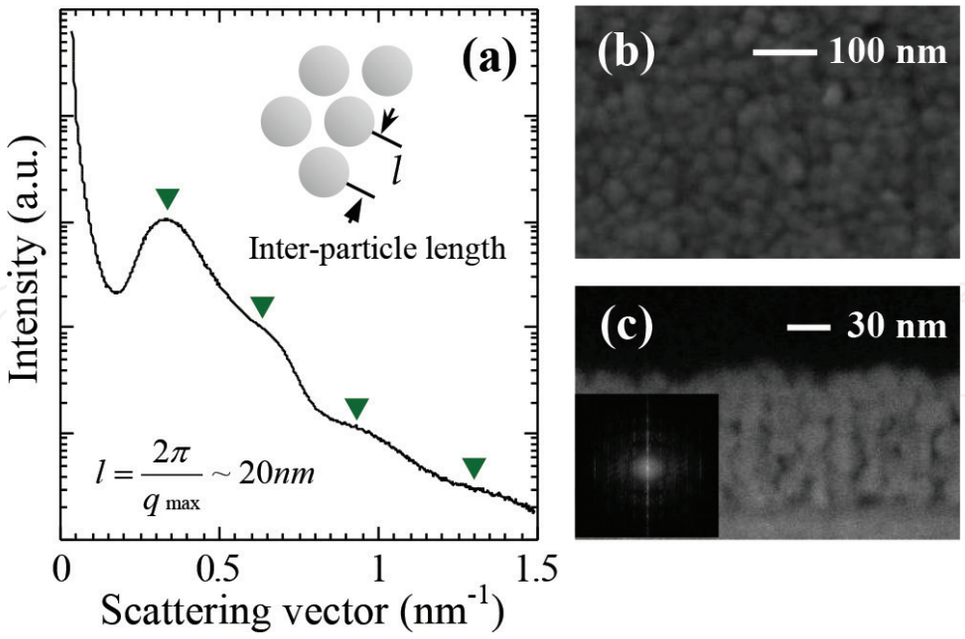

Figure 5. (a) SAXS pattern of a 96 nm-thick NP sheet. Inset indicates schematic picture to explain an inter-particle length (*l*). (b) In-plane surface (b) and cross-section SEM image (c) of 96 nm-thick NP sheets. Inset represents a FFT pattern of a cross-section SEM image (Figures 5 and 7 of Ref. [39]). Copyright 2014 by the American Chemical Society.

self-organizations of colloidal NPs into a hexagonally close-packed (HCP) structure based on shear and capillary forces on substrates [37, 38] [**Figure 5(b)**]. In addition, a cross-section SEM image also provided a close-packed structure [**Figure 5(c)**]. However, a particle-alignment is disordered packing feature between NPs, as indicated from a fast-Fourier transform (FFT) pattern of the SEM image [inset in **Figure 5(c)**]. This local structure is related to the broadened interferences of SAXS pattern, which gives influences to optical properties of the NP sheets.

5. Infrared optical responses of ITO NP sheets

5.1. Mono-layered NP sheets

The optical properties of a mono-layered ITO NP sheet are shown in **Figure 6**. Transmittance spectra exhibited a resonant peak at 2.64 μm, which revealed the red-shifted resonant wavelength because of a collective plasmon resonance (CPR) effect compared to those of NPs dispersed in toluene [**Figure 6(a)**] [40]. On the other hand, reflectance at the resonant wavelength was very small, indicating that the optical responses were mainly dominated by light absorption properties. Furthermore, the finite-difference time-domain (FDTD) simulation was carried out to evidence the experimental results. The modelled mono-layered NP sheet (R = 20 nm) has a HCP structure with an inter-particle length (l) of 2 nm along the X-Y (in-plane) direction. The modelled NP sheet was illuminated with light directed in the Z-direction from the air side. Periodic boundary conditions were applied to X and Y directions, and the bottom and top of the simulated domain in the Z-direction were analysed using perfectly matched layer (PML) boundary conditions. The refractive index (n) of the surface ligand between NPs was defined

to 1.437. An ellipsometric measurement of an ITO film was conducted to obtain the complex dielectric constants within the visible-IR range. A surface ligand molecular of the NPs was a capric fatty acid in this chapter. A resonant peak at 2.45 μm was reproduced in transmittance and reflectance spectra, which was compared to the experimental results [**Figure 6(b)**]. The CPR effect was excited due to long-range coherences of *E*-field interactions between NPs, as supported from the two-dimensional (2D) image of the E-field distribution [inset of **Figure 6(b)**].

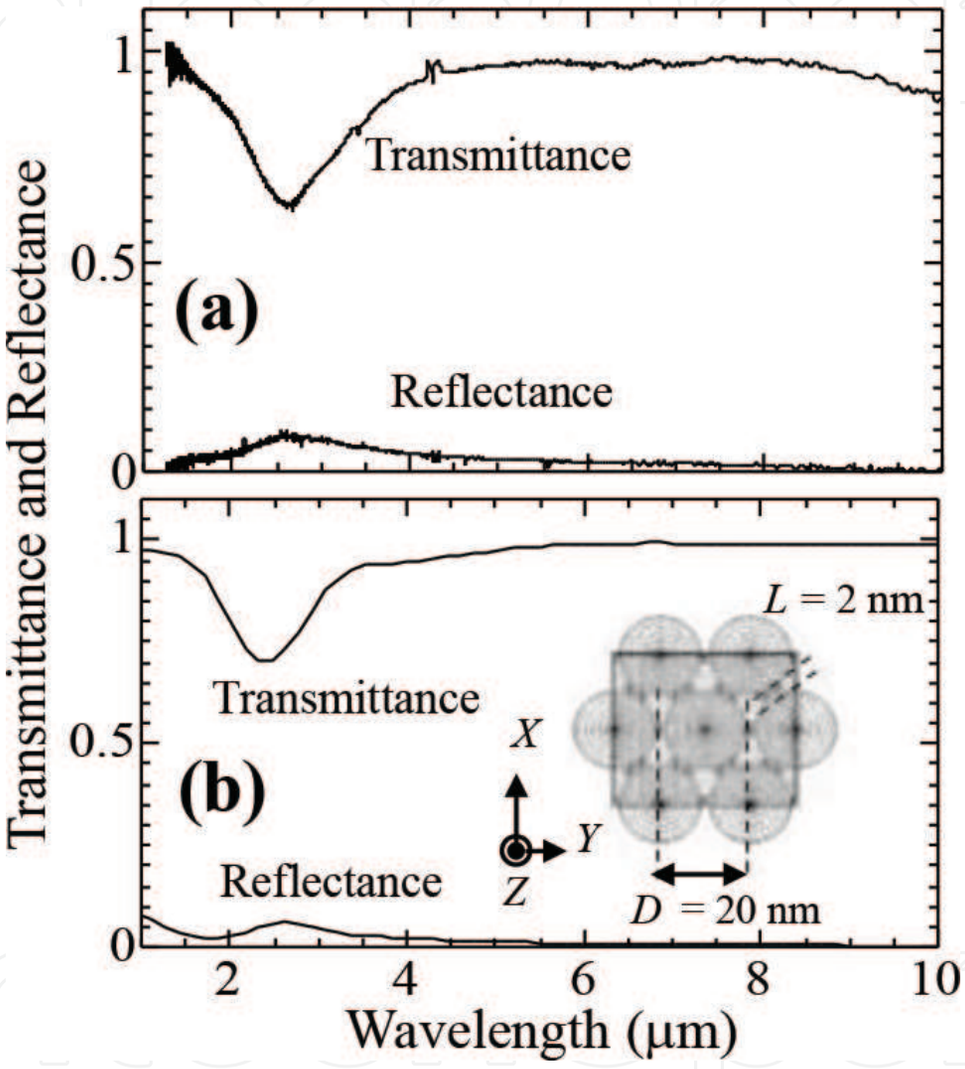

Figure 6. (a) Experimental and (b) simulated transmittance and reflectance of a mono-layered NP sheet with a HCP structure. Inset in Figure 6(b) shows a model of a mono-layered NP sheet and an *E*-field distribution when an electric field of light is applied along the *X*-direction (Figure 4 of Ref. [39]). Copyright 2014 by the American Chemical Society.

5.2. Three-dimensional NP sheets

3D-stacked NP sheets showed a remarkable change in optical properties, which were clearly found on transmittance and reflectance spectra [**Figure 7(a)** and **(b)**]. Transmittance with a resonant wavelength at 2.20 μm decreased to a level close to zero with increasing sheet thickness. On the other hand, reflectance was enhanced at a close proximity of 0.6 in terms to the

http://dx.doi.org/10.5772/67588

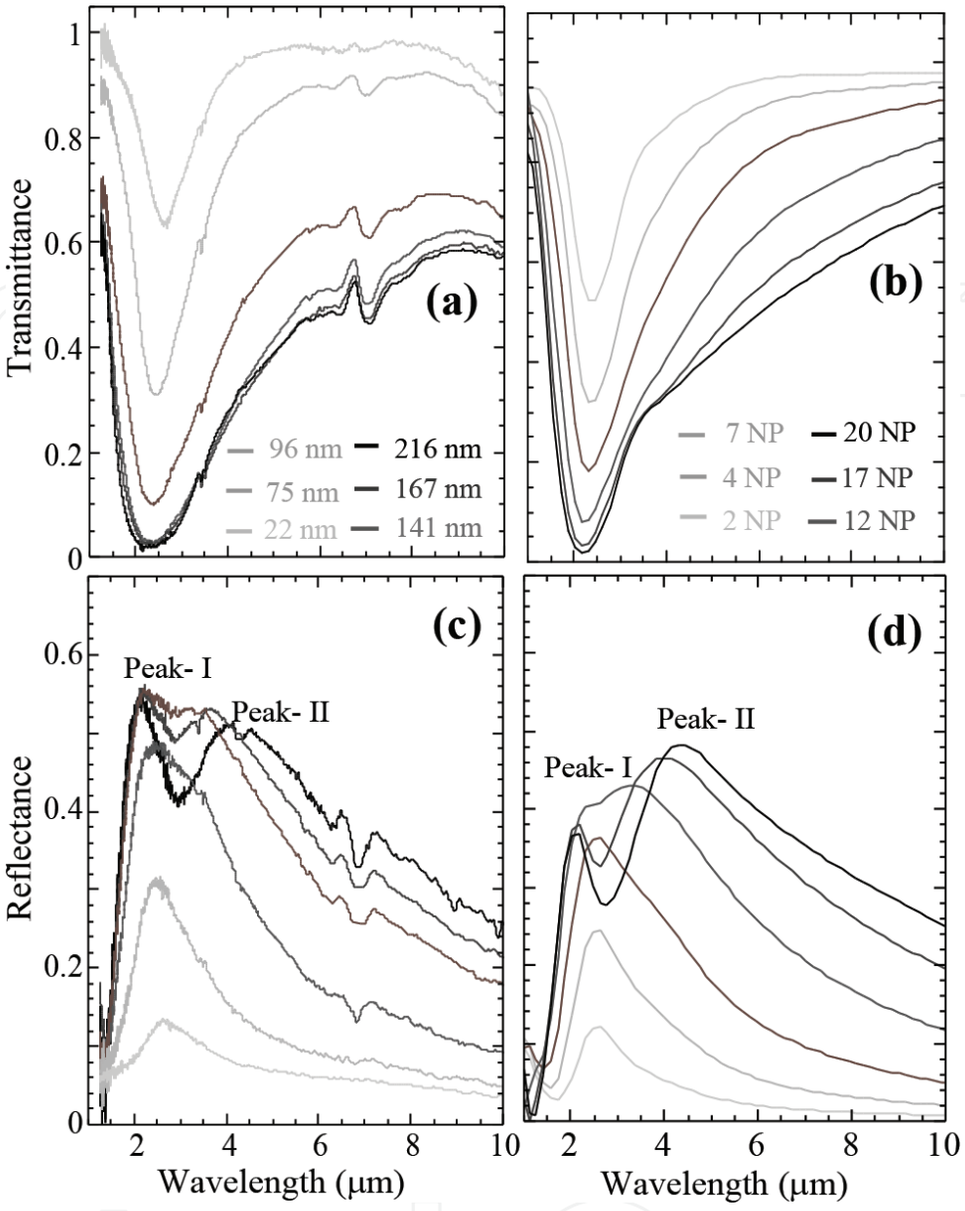

Figure 7. (a) Experimental and (b) simulated transmittance spectra of NP sheets with different thicknesses. (c) Experimental and (d) reflectance spectra of NP sheets with various NP layers. The modeled NP sheet was illuminated with light directed in the *Z*-direction from the air side. The direction of the *E*-field was perpendicular to the light and parallel to the *X*-direction (Figure 5 of Ref. [39]). Copyright 2014 by the American Chemical Society.

sheet thickness [**Figure 8(b)**]. The single peak of 22 nm-thick NP sheet was gradually separated into lower and higher wavelengths with the sheet thickness [**Figure 8(a)**]. We observed two types of resonant peaks (I and II) at 2.13 and 4.02 μm in the near- and mid-IR region on the 216 nm-thick NP sheet, respectively. The ratio of (*R*/*A*) of reflectance (*R*) and absorbance (*A*) increased quickly to a large value with increasing sheet thickness, which indicated that the assembled NP sheets showed reflectance-dominated optical properties.

FDTD calculations were conducted in order to clear the experimental results. From the cross-section SEM image, the modelled NP layers are based on a 3D HCP structure with an *l* value

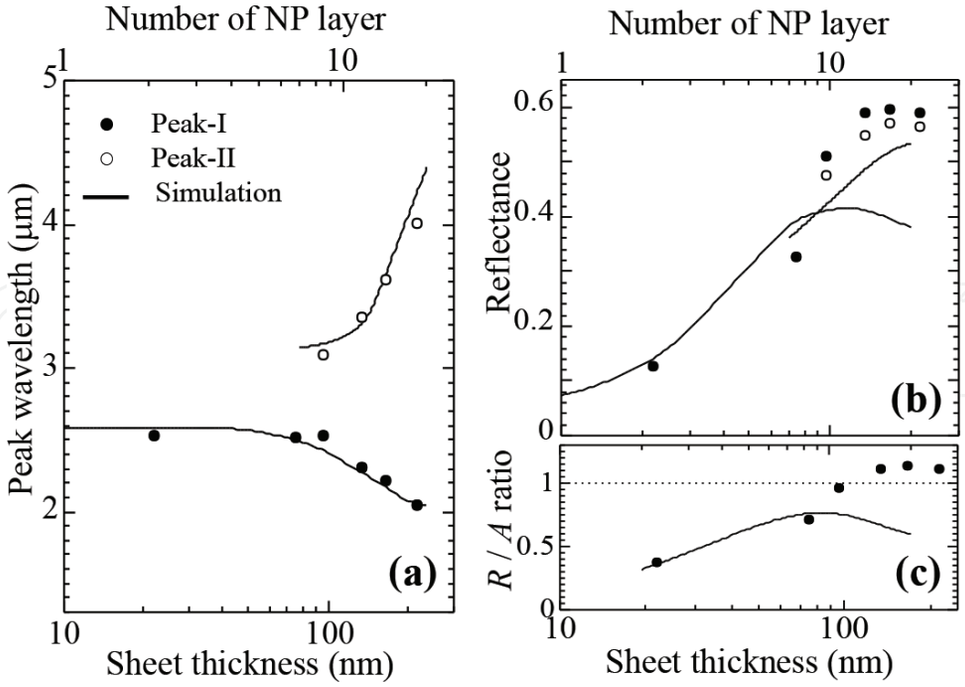

Figure 8. (a) Resonant wavelengths and (b) reflectance of peak-I and peak-II as a function of sheet thickness (bottom horizontal axis) and number of NP layers (upper horizontal axis). Black lines indicate calculated results of FDTD simulations. (c) Experimental and calculated ratios of *R*/*A* at peak position related to peak-I. *R* and *A* represent reflectance and absorbance, respectively (Figure 6 of Ref. [39]). Copyright 2014 by the American Chemical Society.

of 2 nm in the *Z*- (out-of-plane) direction. A layer structure along the in-plane (*X*-*Y*) direction employed the mono-layered NP layer in Section 5.1. The systematic change in the number of NP layers from 1 to 20 was capable of reproducing the experimental spectra [**Figure 7(c)** and **(d)**]. The employed model could describe the optical properties of the NP sheets. The increase in number of NP layers provided the resonant peaks in transmittance and peak separations in reflectance. These behaviours were similar to the experiment results [**Figure 8(a)** and **(b)**]. Herein, the reflectance for peak-I was smaller than that for peak-II in the case of calculations, resulting in a difference of *R*/*A* ratio between experimental and calculation aspects [**Figure 8(c)**].

5.3. Plasmon hybridization and reflectance mechanism

The resonant origins of reflectance of peak-I and peak-II were theoretically examined as a function of interparticle length between NPs. **Figure 9(a)** exhibits calculated reflectance of NP sheets with different *l* values on the basis of 20 NP layer model, revealing that reflectance monotonically enhanced with decreasing *l*. Peak-II showed a red-shift to longer wavelengths when decreasing *l* from 10 to 1 nm. In contrast, peak-I remained unchanged [**Figure 9(b)**]. These results suggest a difference in the origin of plasmon resonance between peak-I and peak-II. In general, the localized *E*-field from each metal NP usually overlaps when metal NPs are closely positioned, and plasmon coupling occurs [41]. In the plasmon hybridization process, the plasmon interaction can be categorized into bonding and anti-bonding levels. For example, the bonding level shows a red-shift of a resonant wavelength with decreasing interparticle length. On the other hand, there is a slight blue-shift a resonant peak is due to

http://dx.doi.org/10.5772/67588

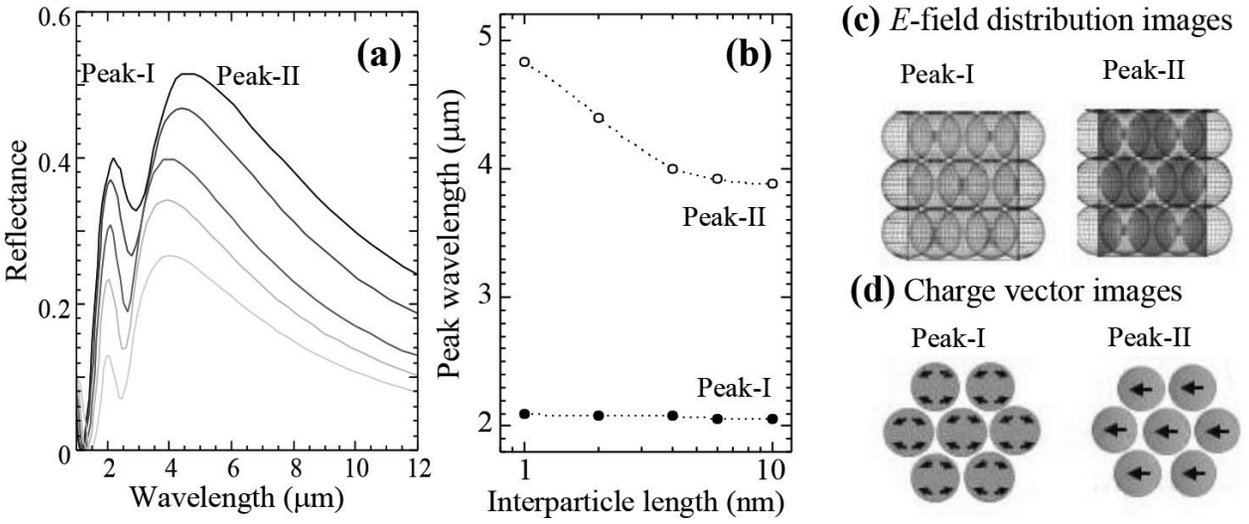

Figure 9. (a) Calculated reflectance of NP sheets with different interparticle lengths. (b) Resonant peaks of peak-I and peak-II as a function of interparticle length. (c) Images of *E*-field distributions. (d) Images of charge vectors at peak-I and peak-II (Figure 6 of Ref. [39]). Copyright 2014 by the American Chemical Society.

the anti-boding level. The peak shifts at peak-I and peak-II were similar to the anti-bonding and bonding states, respectively. Furthermore, *E*-field distributions and their charge vectors were investigated at peak-I and peak-II [**Figure 9(c)** and **(d)**]. We firstly focus on the mid-IR reflectance at peak-II. A resonant mode comprised of individual dipolar plasmons oscillating in-phase along the direction of incident polarization. The *E*-fields between the NPs were only localized along the in-plane *X*-direction. On the other hand, field analysis at peak-I exhibited that the dipolar plasmons in the NPs oscillate out-of-phase, providing a net dipole moment of nearly zero. Their *E*-fields were coupled with surrounding NPs along the out-of-plane and in-plane directions. The mode splitting of plasmon resonances was related to 3*D*-stacked assemblies of NPs. Accordingly, quadrupole and dipole modes were formed as peak-I and peak-II, respectively. These behaviours became pronounced with an increase in sheet thickness. We note that the differences in reflectance between experimental and simulation data could be considered in relation of a local structure and plasmon resonance. The NP sheets had a disordered structure of NPs from the SEM image. A dipole mode can be strongly observed in precise close-packed NP assemblies.

The character of *E*-field coupling in the NP sheets was further studied from polarized reflectance measurements. Two types of light polarized perpendicular (*s*-polarized) and parallel (*p*-polarized) to the plane of incidence were introduced the sample at an incident angle of 75°. **Figure 10** shows polarized reflectance spectra for *s*- and *p*-polarization configurations for a NP sheet. In a case of *s*-polarization, peak-I and peak-II were simultaneously obtained because the electric vector of the radiation produced electron oscillations in NPs parallel to the in-plane of the sample. On the other hand, peak-I only found for a *p*-polarization case. These optical properties concerning both polarizations are explained as follows.

The electric vector excites electron oscillations in NPs normal to the plane of the sample, and suppresses the *E*-field coupling along the in-plane direction. These results revealed that

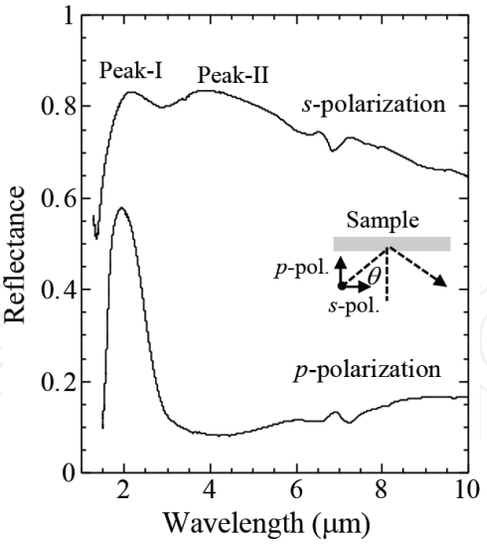

Figure 10. Reflectance spectra of a 216 nm-thick NP sheet for s- and p-polarized lights. Inset indicates the direction of the electric vector of incident light in addition to an *E*-field distribution under a *p*-polarization.

peak-II was excited by the field coupling along the in-plane directions. In contrast, the reflectance at peak-I was essential for *E*-field coupling along the out-of-plane direction. That is, the near- and mid-IR reflectance of the NP sheets was attributed to the 3*D* field coupling along the out-of-plane and in-plane directions. The film thickness-dependent plasmon splitting was attributed to the formation of field coupling along the out-of-plane direction, leading to the enhanced reflectance in the near-IR range.

5.4. Nanoparticle gap and reflectance of ITO NP sheets

The thermal behaviours of the NP samples were investigated by TG-DTA in an N_2 atmosphere with a heating rate of 10°C/min. The weight loss up to 250°C might be related to the loss of physically or chemically absorbed water. There was an obvious weight loss in the temperature range 270–320°C because of the generation of organic species confirmed by *m*/*z* peaks at 18 (H_2O) and 44 (CO_2, C_3H_8, C_2H_4O *etc*.) [**Figure 11(a)** and **(b)**]. The decomposed species were owing to thermal removal of the surface ligands composed of fatty acids on the NP surfaces. There phenomena are identified by FT-IR measurements. The relation between surface ligand molecules and optical properties in the NP sheets was cleared by the spectral changes after annealing at different temperatures (T_A = 150–550°C). **Figure 11(c)** shows temperature-dependent reflectance spectra taken in an inert atmosphere for a 216 nm-thick NP sheet, revealing remarkable spectral changes with increasing temperature. The two resonant peaks at 150°C were weakened gradually following the change in spectral shape with increasing temperature. Above all, the near-IR reflection at peak-I shifted to longer wavelengths at high temperatures above 300°C corresponding to the removal of the surface ligands. In addition, the annealing effects of NP sheets were checked by the electrical resistivity in the sheets. Electrical resistivity was in the order of $10^4\Omega$.cm below annealing temperatures below 250°C because the presence of the surfactant layers on NPs seriously impedes carrier transport in the NP sheets. The surface ligands act as interparticle insulating layers in NP networks [42].

http://dx.doi.org/10.5772/67588

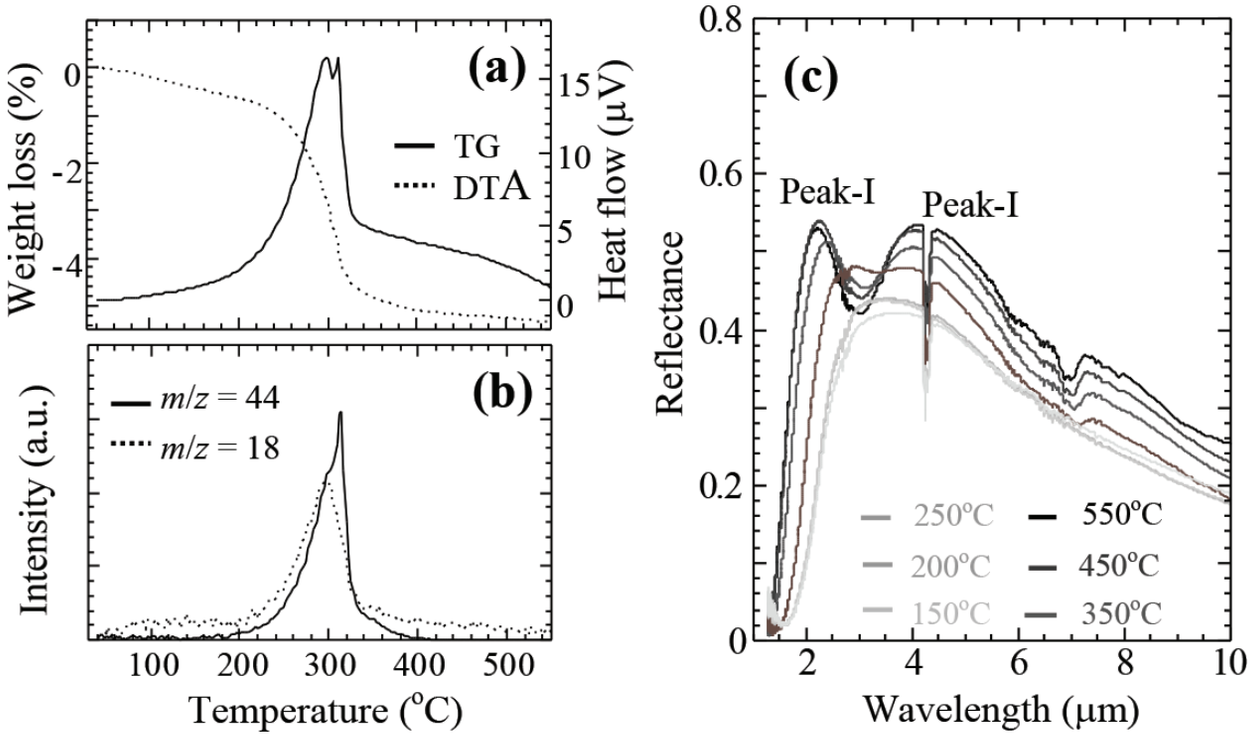

Figure 11. (a) TG-DTA curves of ITO NP samples in an N_2 atmosphere. (b) TOF-Mass spectroscopy combined with TG-DTA. *M/z* signals at 18 and 44 were detected in the range 27–550°C. (c) Dependence of reflectance spectra on annealing temperature for a 216 nm-thick NP sheet.

However, this was markedly reduced at high temperatures above 350°C due to the removal of the surface ligands. Therefore, the removal of surface ligand molecules from the NPs strongly affected the whole reflective phenomena, which also clarified the importance of interparticle length in obtaining a high reflectance performance.

5.5. Electromagnetic responses in microwave range

EM properties are shortly discussed on a NP sheet in the microwave range 0.5–40 GHz. This range is an important frequency range for telecommunications. Transparent solar-thermal shielding is effective techniques to prevent room heat in order to realize comfortable environment in vehicles. However, it is strongly required for vehicles to transmit EM waves in the microwave range through windows to carry out radio communications such as an Electronic Toll Collection System (ETC) and Information traffic system (ITS). Therefore, it is important to measure EM properties of NP sheets in addition to evaluate optical properties in the IR range.

250 nm-thick NP sheet with an A4 size was fabricated on a PET substrate (thickness: 0.2 mm) using a roll-coating method [inset of **Figure 12(a)**]. High reflectance with a close proximity of 0.6 was also obtained on a flexible PET substrate [**Figure 12(a)**]. The shielding effectiveness (SE) of the flexible NP sheet was almost zero, as different from that of a RF sputtered ITO film [**Figure 12(b)**]. The difference between the two materials related to electrical conductance (σ) in the sheets, which was in the order of 10^{-5} and 10^{-3} S/cm for the NP sheet and sputtered film, respectively. If the shielding material is thin, SE is mainly dominated by EM reflection as follows [43]:

$$SE = 20\log(\sqrt{2}\,\beta_0/2R) \tag{10}$$

where, β_0^2 is μ/ε_0, and R is the sheet resistivity (=1/σ). The significant obstruction of electron carrier transport between NPs produced low electrical conductance because of the presence of surface ligands on the NPs, and realized the high microwave transmissions.

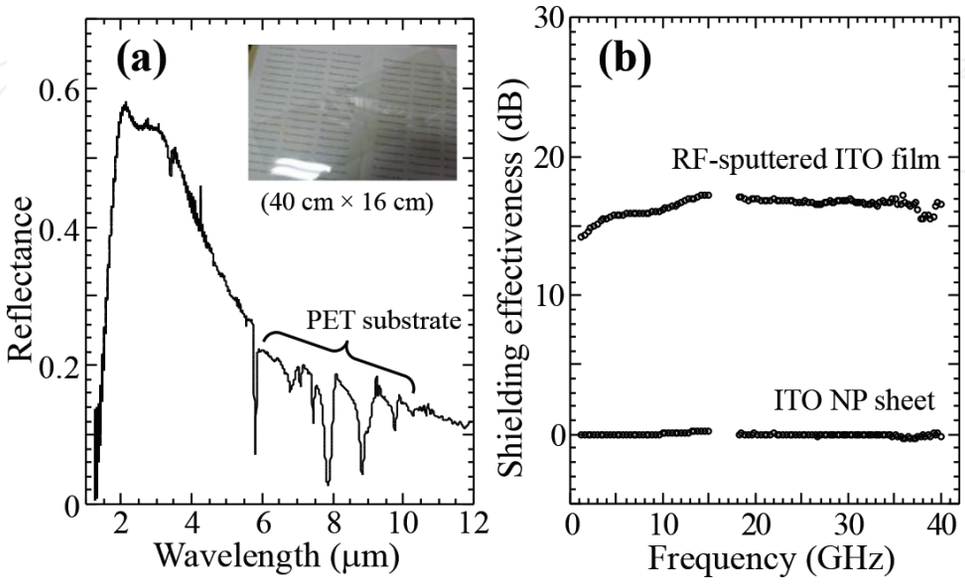

Figure 12. (a) Reflectance of a NP sheet on a PET film. Inset image represents a photograph of the fabricated sheet sample. (b) Shielding effectiveness (SB) in the microwave range 0.5–40 GHz for a NP sheet and RF-sputtered ITO film.

ITO NPs were used to obtain assembled NP sheets with small interparticle lengths by the presence of ligand molecules on the particle surfaces. This situation produced effective *E*-field coupling along the in-plane and out-of-plane directions. This caused the plasmon hybridization for the quadrupole and dipole modes, which played an important role in producing the high reflectance in the near- and mid-IR range. In addition, the *E*-field enhancements between NPs simultaneously caused a remarkable reduction of electrical contacts between the NPs, which contributed to the high microwave transmissions. The plasmonic control in assemblies of NPs represents promising potential for structural and optical designs used to fabricate a flexible thermal-shielding sheet with a reflection-type based on transparent oxide semiconductors. The knowledge gained in this study can be applied to NP sheets utilizing inexpensive ZnO and WO_3 [44, 45].

6. Summary

Crystallinity and local structures of oxide semiconductor NPs were conducted using ITO NPs by XRD and TEM measurements in Section 2. The plasmonic resonances of ITO NPs were clearly obtained in the near-IR range from the viewpoints of optical and EELS signals. In particular, electron-impurity scattering contributed towards plasmon damping as one of a factor that is absent in metal NPs on the basis of theoretical and experimental approaches, which

was discussed in Section 3. In Sections 4 and 5, we described IR plasmonic applications in ITO NP sheets for solar-thermal shielding technology. Above all, the *E*-field coupling between NPs produced interesting plasmonic coupling because of the creation of narrow crevices in the interparticles. 3*D* field interactions along the in-plane and out-of-plane directions caused high reflectance in the near- and mid-IR regions. Finally, ITO NP sheets could be extended to obtain large-size flexible films on PET substrates, which simultaneously showed microwave transmittance essential for telecommunications.

The above results provided important insights for basic science and practical applications based on plasmonic investigations based on oxide semiconductor NPs. However, plasmonic properties and applications are stand still-points at the present time. Hereafter, it will be needed to study plasmonic phenomena on oxide semiconductor NPs towards new concepts concerning optical manipulations in the IR range.

Acknowledgements

This research was supported in part by a grant-in-Aid from the JSPS Core-to-Core Program, A. Advanced Research Network, a grand from Toyota Physical and Chemical Research Institute, and for a grant-in-Aid for Exploratory Research and Scientific Research (B).

Author details

Hiroaki Matsui[1,2]* and Hitoshi Tabata[1,2]

*Address all correspondence to: hiroaki@ee.t.u-tokyo.ac.jp

1 Department of Bioengineering, the University of Tokyo, Japan

2 Department of Electric Engineering and Information Systems, the University of Tokyo, Japan

References

[1] C. Rhodes, M. Cerruti, A. Efremenko, M. Losego, D. E. Aspnes, J. -P. Maria and S. Franzen. Dependence of plasmon polaritons on the thickness of indium tin oxide thin films. Journal of Applied Physics. 2008;**103**:093108(1)–093108(8). doi:10.1063/1.2908862.

[2] H. Matsui, W. Badalawa, A. Ikehata and H. Tabata. Oxide surface plasmon resonance for a new sensing platform in the near-infrared range. Advanced Optical Materials. 2003;**1**:397–403. doi:10.1002/adom.201200075.

[3] W. Badalawa, H. Matsui, A. Ikehata and H. Tabata. Surface plasmon modes guided by Ga-doped ZnO layers bounded by different dielectrics. Applied Physics Letters. 2011;**99**:011913(1)–011913(3). doi:10.1063/1.3608313.

[4] E. Sachet, M. D. Losego, J. Guske, S. Franzen and J. -P. Maria. Mid-infrared surface plasmon resonance in zinc oxide semiconductor thin films. Applied Physics Letters. 2013;**102**:051111(1)–051111(4). doi:10.1063/1.4791700.

[5] H. Matsui, A. Ikehata and H. Tabata. Surface plasmon sensors on ZnO: Ga layer surfaces: Electric-field distributions and absorption-sensitive enhancements. Applied Physics Letters. 2015;**106**:019905(1)–019905(5). doi:10.1063/1.4905211.

[6] Y. Zhao, H. Pan, Y. Lou, X. Qiu, J. J. Zhu and C. Burda. Plasmonic $Cu_{2-x}S$ nanocrystals: Optical and structural properties of copper-deficient copper (I) sulfides. Journal of the American Chemistry Society. 2009;**131**(12):4253–4261. doi:10.1021/ja805655b.

[7] G. Garcia, R. Buonsanti, E. L. Runnerstrom, R. J. Mendelsberg, A. Llordes, A. Anders, T. J. Richardson and D. J. Milliron. Dynamically modulating the surface plasmon resonance of doped semiconductor nanocrystals. Nano Letters. 2011;**11**(10):4415–4420. doi:10.1021/nl202597n.

[8] G. V. Naik, V. M. Shalaev and A. Boltasseva. Alternative plasmonic materials: Beyond gold and silver. Advanced Materials. 2013;**25**(24):3264–3294. doi:10.1002/adma201205076.

[9] T. Yamada, H. Makino, N. Yamamoto and T. Yamamoto. Ingrain and grain boundary scattering effects on electron mobility of transparent conducting polycrystalline Ga-doped ZnO films. Journal of Applied Physics. 2010;**107**:123534(1)–123534(8). doi:10.1063/1.3447981.

[10] C. Sonnichesen, T. Franzl, T. Wilk, G. von Plessen and J. Feldmann. Plasmon resonances in large noble-metal clusters. New Journal of Physics. 2002;**4**:93(1)–93(8). doi:S1367-2630(02)39458-8.

[11] Z. C. Jin, I. Hamberg and C. G. Granqvist. Optical properties of sputter-deposited ZnO: Al thin films. Journal of Applied Physics. 1988;**64**:5117–5131. doi:10.1063/1.342419.

[12] N. Yamamoto, H. Makino, S. Osone, A. Ujihara, T. Ito, H. Hokari, T. Maruyama and T. Yamamoto. Development of Ga-doped ZnO transparent electrodes for liquid crystal display panels. Thin Solid Films. 2012;**520**(12):4131–4138. doi:10.1016/j/tsf.2011.04.067.

[13] S. Q. Li, P. Guo, B. Buchholz, W. Zhou, Y. Hua, T. W. Odom, J. B. Ketterson, L. E. Ocola, K. Sakoda and R. P. H. Chang. Plasmon-photonic mode coupling in indium-tin-oxide nanorod arrays. ACS Photonics. 2014;**1**(3):163–172. doi:10.1021/ph400038g.

[14] D. B. Tice, S. Q. Li, M. Taglazucchi, D. B. Buchholz, E. A. Weiss and R. P. H. Chang. Ultrafast modulation of the plasma frequency of vertically aligned indium tin oxide rods. Nano Letters. 2014;**14**(3):1120–1126. doi:10.1021/nl4028044.

[15] S. Wuestner, J. M. Hamm, A. Pusch, O. Hess. Plasmonic leaky-mode lasing in active semiconductor nanowires. Laser & Photonics Reviews. 2015;**9**(2):256–262. doi:10.1002/por.201400231.

[16] S. D. Lounis, E. L. Runnerstrom, A. Llordés and D. J. Milliron. Defect chemistry and plasmon physics of colloidal metal oxide nanocrystals. Journal of Physical Chemistry C. 2014;**5**:1564–1574. doi:10.1021/jz500440e.

[17] A. M. Schimpf, S. D. Lounis, E. L. Runnerstrom, D. J. Milliron and D. R. Gamelin. Redox chemistries and plasmon energies of photodoped In_2O_3 and Sn-doped In_2O_3 (ITO) nanocrystals. Journal of American Chemistry Society. 2014;**137**:518–524. doi:10.1021/a5116953.

[18] D. Solis Jr., A. Paul, J. Plson, L. S. Slaughter, P. Swanglap, W. S. Chang and S. Link. Turning the corner: Efficient energy transfer in bent plasmonic nanoparticle chain waveguides. Nano Letters. 2013;**13**(10):4779–4784. doi:10.1021/nl402358h.

[19] N. Tognalli, A. Fainstein, E. Calvo, C. Bonazzola, L. Pietrasanta, M. Campoy-Quiles and P. Etchegoin. SERS in PAH-Os and gold nanoparticle self-assembled multilayers. The Journal of Chemical Physics. 2005;**123**:044707(1)–044707(9). doi:10.1063/1.1954707.

[20] M. Fan, M. Thompson, M. L. Andreade and G. Brolo. Silver nanoparticles on a plastic platform for localized surface plasmon resonance biosensing. Analytical Chemistry. 2010;**82**(15):6350–6352. doi:10.1021/ac101495m.

[21] A. Furube, T. Yoshinaga, M. Kanehara, M. Eguchi and T. Teranishi. Electric-field enhancement inducing near-infrared two-photon absorption in an indium-tin oxide nanoparticle film. Angewandte Chemie. 2012;**51**(11):2640–2642. doi:10.1002/anie20117450.

[22] H. Matsui, W. Badalawa, T. Hasebe, S. Furuta, W. Nomura, T. Yatsui, M. Ohtsu and H. Tabata. Coupling of Er light emissions to plasmon modes on In_2O_3: Sn nanoparticle sheets in the near-infrared range. Applied Physics Letters. 2014;**105**(4):041903(1)–041903(5). doi:10.1063/1.4892004.

[23] K. Okamoto, B. Lin, K. Imazu, A. Yoshida, K. Toma, M. Toma and K. Tamada. Tning colors of silver nanoparticle sheets by multilayered crystalline structures on metal substrates. Plasmonics. 2012;**8**(2):581–590. doi:10.1007/s11468-012-9437-2.

[24] F. Le, D. W. Brandl, Y. A. Urzhumov, H. Wang, J. Kundu, N. J. Halas, J. Aizpurua and P. Nordlander. Metallic nanoparticle arrays: A common substrate for both surface-enhanced Raman scattering and surface-enhanced infrared absorption. ACS Nano. 2008;**2**(4):707–718. doi:10.1021/nn800047e.

[25] K. Okamoto, I. Niki, A. Scherer, Y. Narukawa. T. Mukai and Y. Kawakami. Surface plasmon enhanced spontaneous emission rate of InGaN/GaN quantum wells probed by time-resolved photoluminescence spectroscopy. Applied Physics Letters. 2005;**87**:071102(1)–071102(3). doi:10.1063/1.2010602.

[26] I. Hamberg and C. G. Granqvist. Evaporated Sn-doped In_2O_3 films: Basic optical properties and applications to energy-efficient windows. Journal of Applied Physics. 1986;**60**:R123–R157. doi:10.1063/1.337534.

[27] S. Y. Li, G. A. Nilsson and C. G. Granqvist. Plasmon-induced near-infrared electrochromism based on transparent conducting nanoparticles: Approximate performance limits. Applied Physics Letters. 2012;**101**:071903(1)–071903(3). doi:10.1063/1.4739792.

[28] K. Katagiri, R. Takabatake and K. Inumaru. Robust infrared-shielding coating films prepared using perhyropolysilazane and hydrophobized indium tin oxide nanoparticles

with tuned surface plasmon resonance. ACS Applied Materials & Interfaces. 2013;**5**(3):10240–10245. doi:10.1021/am403011t.

[29] X. Fang, C. L. Mak, J. Dai, K. Li, H. Ye and C. W. Leung. ITO/Au/ITO sandwich structure for near-infrared plasmonics. ACS Applied Materials & Interfaces. 2014;**6**(18):15743–15752. doi:10.1021/am5026165.

[30] P. Tao, A. Viswanath, L. S. Schadler, B. C. Benicewica and R. W. Siegel. Preparation and optical properties of indium tin oxide/epoxy nanocomposites with polyglycidyl methacrylate grafted nanoparticles. ACS Applied Materials & Interfaces. 2011;**3**(9):3638–3645. doi:10.1021/am200841n.

[31] Z. Sun, J. He, A. Kumbhar and J. Fang. Nonaqueous synthesis and photoluminescence of ITO nanoparticles. Langmuir. 2010;**26**(6):4246–4250. doi:10.1021/la903316b.

[32] H. Matsui, S. Furuta and H. Tabata. Role of electron carriers on local surface plasmon resonances in doped oxide semiconductor nanocrystals. Applied Physics Letters. 2014;**104**(12):211903(1)–211903(4). doi:10.1063/1.4880356.

[33] J. A. School, A. L. Koh and J. A. Dionne. Quantum plasmon resonances of individual metallic nanoparticles. Nature. 2012;**483**:421–427. doi:10.1038/nature10904.

[34] G. V. Hartland. Optical studies of dynamics in noble metal nanostructures. Chemistry Reviews. 2011;**111**(6):3858–3887. doi:10.1021/cr1002547.

[35] D. Ross and R. Aroca. Effective medium theories in surface enhanced infrared spectroscopy: The pentacene example. Journal of Chemical Physics. 2002;**117**:8095–8103. doi:10.1063/1.1502656.

[36] A. Pflug, V. Sitinger, F. Ruske, B. Szyszka and G. Dittmar. Optical characterization of aluminium-doped zinc oxide films by advanced dispersion theories. Thin Solid Films. 2004;**455–456**:201–206. doi:10.1016/j.tsf.2004.01.1006.

[37] S. M. Yang, S. G. Jang, D. G. Chio, S. Kim and H. K. Yu. Nanomachining by colloidal lithography. Small. 2006;**2**(4):458–475. doi:10.1002/smll.200500390.

[38] P. Jiang and M. J. McFarland. Large-scale fabrication of wafer-size colloidal crystals, macroporous polymers and nanocomposites by spin-coating. Journal of the American Chemistry of Society. 2004;**126**(42):13778–13786. doi:10.1021/ja0470923.

[39] H. Matsui, S. Furuta, T. Hasebe and H. Tabata. Plasmonic-field interactions at nanoparticle interfaces for infrared thermal-shielding applications based on transparent oxide semiconductors. ACS Applied Materials & Interfaces. 2016;**8**(18):11749–11759. doi:10.1021/acsami6b1202.

[40] C. Jiang, S. Markutsya and V. V. Tsukruk. Collective and individual plasmon resonances in nanoparticle films obtained by spin-assisted layer-by-layer assembly. Langmuir. 2003;**20**(3):882–890. doi:10.1021/la0355085.

[41] P. Nordlander, C. Oubre, E. Prodan, K. Li and M. I. Stockman. Plasmon hybridization in nanoparticle dimers. Nano Letters. 2004;**4**(5):899–903. doi:10.0121/nl049681c.

[42] J. Y. Kim and N. A. Kotov. Charge transport dilemma of solution-processed nanomaterials. Chemistry of Materials. 2014;**26**(1):134–152. doi:10.1021/cm402675k.

[43] C. A. Klein. A microwave shielding effectiveness of EC-coated dielectric slabs. IEEE Transactions of Microwave Theory Techniques. 1990;**38**:321–324.

[44] C. Guo, S. Yin, M. Yan, M. Kobayashi and T. Sato. Morphology-controlled synthesis of $W_{18}O_{49}$ nanostructures and their near-infrared absorption properties. Inorganic Chemistry. 2012;**51**(8):4763–4771. doi:10.1021/in300049j.

[45] H. Matsui, L. Y. Ho, T. Kanki, T. Tanaka, J. J. Delaunay and H. Tabata. Mid-infrared plasmonic resonances in two-dimensional VO_2 nanosquare arrays. Advanced Optical Materials. 2013;**3**:1759–1767.

IntechOpen